Chapter 3

A Single Heterojunction n-i-p Photodetector Based on Mercury Cadmium Telluride for Terahertz Applications

3.1 Introduction

The Terahertz region is the frequency range which mostly remain unexplored for possible telecommunication or non-telecommunication applications. The characteristics of the THz wave and its possibility in many applications makes its study very interesting [61], [119]. The potential applications of the terahertz radiation include wireless communication, radio astronomy, medical imaging, dentistry, pharmaceuticals, detection of flaws in the machinery, security screening, quality assurance, ozone layer monitoring, explosive detection, etc. [119], [120]. But the research in the terahertz region remains still unearthed due to the absence of good sources and detectors. As discussed in the previous chapters, there are several technological challenges in the generation and the detection of the THz radiation. A very few technologically mature solutions are available to fully exploit this potential. Specifically, there is a need for the development of efficient and dependable photodetectors that can be used for the terahertz detection. Over the past few decades, there were contributions in designing and fabricating devices based on II-VI compound materials for a variety of applications. Devices made of narrow bandgap materials are favoured in detection of the terahertz radiation. Of all the available narrow bandgap materials, HgCdTe is best suited for THz detection since its bandgap can be tailored over a region to operate in the wavelength from 1 µm-30 µm. HgCdTe based detectors need to be operated below room temperature to suppress the effects of thermally generated carriers for achieving high detectivity. A reliable terahertz detector based on HgCdTe beyond 10 µm would be a significant advantage in attaining wide range of applications. The experimental investigations and the technology required for the development of the THz detectors are too costly. Also, it is very much essential to develop an optimized device that possesses good optical characteristics. So, optimized THz detectors may be developed by theoretical modeling and verification through numerical simulation that involves less cost. The theoretical results will help the design engineers to fabricate the detector with a minimal number of experimental trials. There are many works reported on HgCdTe based detectors for the mid wavelength infrared and the long wavelength infrared strategic atmospheric windows [115]-[116], [122]-[123]. But very a few works have been reported using the devices made of HgCdTe material for the THz detection [117]-[118]. It is understood that p-i-n diodes exhibit a better optoelectronic characteristics as compared to the p-n diodes. In this chapter, a single heterojunction photodetector $N^{+} - CdTe/\, n^{0} - Hg_{0.824675}Cd_{0.175325}Te\,/p^{+} - Hg_{0.824675}Cd_{0.175325}Te$ n-i-p photodetector has been proposed and analyzed to examine its suitability as a THz detector. The electrical and the optical characteristics of the proposed device have been simulated with the help of ATLAS™ simulation tool at an operating wavelength of 30 µm. The analytical simulation has also been performed using closed-form expressions. For electrical and optical characterization, the model equations have been solved under appropriate boundary conditions. The results obtained on the basis of ATLAS simulation are subsequently validated by the results of analytical model.

3.2 Proposed device structure

The proposed structure shown in Fig.3.1 comprises a heavily doped $N^{+} - CdTe$ (window layer) over a lightly doped $n^{0} - Hg_{1-x}Cd_{x}Te$ (active layer) which is virtually grown on a $p^{+} - Hg_{1-x}Cd_{x}Te$ on a suitable substrate like $CdZnTe$. The parameters d_n, d_p, t are the thicknesses of $N^{+} - CdTe$ layer, $p^{+} - Hg_{1-x}Cd_{x}Te$ layer and $n^{0} - Hg_{1-x}Cd_{x}Te$ layer respectively. The quantities x_n and x_p are the depletion region widths in the active layer and p^{+} regions respectively. The photodetector operates under the reverse bias condition. The active layer doping concentration has to be kept as low as possible in *HgCdTe* photodiodes in order to minimize the recombination and maximize the minority carrier diffusion length. Large carrier concentration in the active layer of *HgCdTe* photodiodes can result in significant Auger processes and reduced minority carrier diffusion length. The N^{+} and p^{+} regions collect most of the photogenerated carriers as the carrier lifetimes are high because of the low doping level of the active layer. Proper selection of the doping, Cd concentrations for the active layer, and the window layer is crucial to control the dark current in the device. The window layer material is chosen to have a wide bandgap to eliminate the contribution of diffusion current. The composition of the material in the active layer determines the cut-off wavelength. The light is presumed to be incident on the top layer. Here, the top layer material is chosen to be *CdTe* since it has a wide bandgap, less lattice mismatch with $Hg_{1-x}Cd_{x}Te$ [124], and it forms a heterojunction with the absorbing layer.

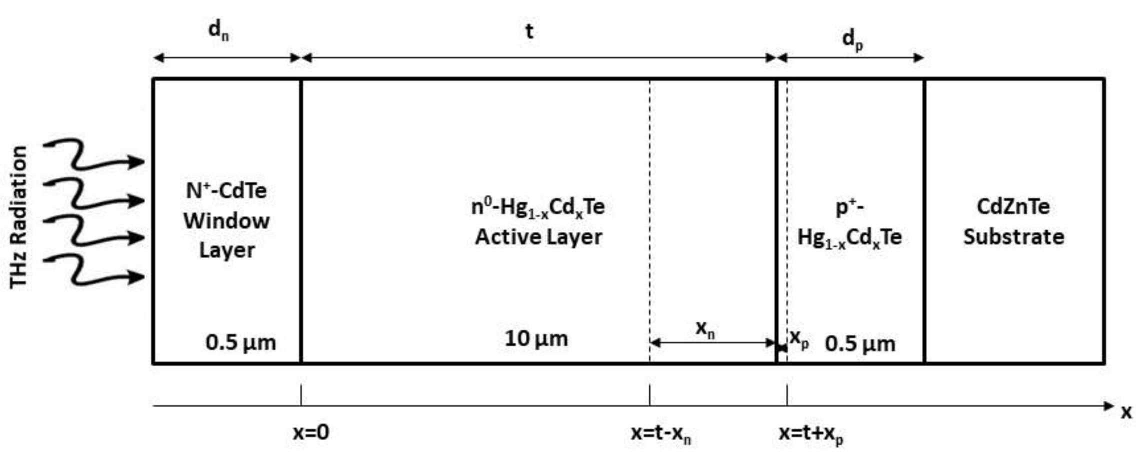

Fig.3.1 Proposed N^{+}-i-p^{+} single heterojunction photodetector

In the present structure, N^+-region is made of a material ($CdTe$) having a larger bandgap (~1.6 eV) than that of the material used in the active region. The N^+-region essentially acts as a window for the incoming long wavelength radiation which is supposed to be absorbed in the active region made of a narrower bandgap material ($Hg_{1-x}Cd_xTe$). As the existing electric field in the active region is very high, the photogenerated carriers are swept across the region very fast to be collected at the respective electrodes. This makes the device work faster than a homojunction p–i–n photodetector. The device is optimized in a way that the entire radiation gets absorbed in the active region and thereby eliminates the possibility of any kind of diffusion of the photogenerated carriers from the neutral region. The device has been assumed to be operated at liquid nitrogen temperature of 77 K.

3.3 Numerical Simulation

The ATLAS™ device simulator uses a Finite Element Method (FEM) to obtain the electrical and optical characteristics of the photodetector. The physics-based model in the simulation tool consists of a set of fundamental equations that link electrostatic potential and carrier densities. The simulation involves the solution to coupled equations using Newton's iteration technique. It consists of Poisson's equation, continuity equation and the transport equations. The solution to these equations is obtained by solving numerically in the ATLAS™ device simulator software for any conventional device.

3.3.1 Poisson's equation

The relationship between the electrostatic potential and the volume of space charge is obtained from the Poisson's equation given by

$$div(\epsilon \nabla \psi) = -\rho \tag{3.1}$$

where ρ is the volume density of space charge, ϵ is the permittivity, ψ is the electrostatic potential, ∇ is the gradient of potential. In 3D cartesian coordinate ∇ is given by

$$\nabla \equiv \mathrm{i}\frac{\partial}{\partial \mathrm{x}} + j\frac{\partial}{\partial \mathrm{y}} + k\frac{\partial}{\partial \mathrm{z}} \tag{3.2}$$

Equation (3.1) for the semiconductor device considered here can be expressed as

$$div(\epsilon\nabla\psi) = -q(p - n + N_D - N_A) \tag{3.3}$$

where N_D is the ionized donor concentration and N_A is the ionized acceptor concentration. The parameters p and n are the concentrations of free holes and electrons in the semiconductor region, q is the charge of the electron.

In ATLAS simulation, the intrinsic Fermi potential is taken as the reference potential.

The electric field ($\mathcal{E}$) is the gradient of the electrostatic potential and is given by

$$\mathcal{E} = -\nabla\psi \tag{3.4}$$

Therefore, equation (3.2) can be expressed as

$$div(\mathcal{E}) = \frac{q}{\epsilon}(N_D - N_A + p - n) \tag{3.5}$$

3.3.2 Continuity Equations

While the above current-density equations are for steady state conditions, the continuity equations deal with time-dependent transport equations which take different forms in different semiconductor devices depending on the mechanism involved in the operation. Qualitatively, the net change of carrier concentration is the difference between the generation and the recombination, plus the net current flowing in and out of the region of interest.

The continuity equations for electrons and holes are given by

$$\frac{\partial n(x,t)}{\partial t} = \frac{1}{q} divJ_n(x,t) + G_n - R_n \tag{3.6}$$

$$\frac{\partial p(x,t)}{\partial t} = -\frac{1}{q} divJ_p(x,t) + G_p - R_p \tag{3.7}$$

where $n(x,t)$ represents the electron concentration, $p(x,t)$ represents the hole concentration, $J_n(x,t)$ is the electron current density and $J_p(x,t)$ is the hole current density at a particular point x and time t, expressed as

$$J_n = q\mu_n n\mathcal{E} + qD_n \frac{dn(x,t)}{dx} \tag{3.8}$$

$$J_p = q\mu_p p\mathcal{E} - qD_p \frac{dp(x,t)}{dx} \tag{3.9}$$

The terms G_n, G_p represent the generation rates of the electrons and holes respectively caused by external influences such as the optical excitation with photons or impact ionization under large electric fields. In the case of study optical illumination (without time variation), the generation rate is expressed as

$$G_{op} = \phi\alpha(\lambda)\exp\left(-\alpha(\lambda)x\right) \tag{3.10}$$

where ϕ is the photon flux density which accounts for the number of photons incident on the device per unit area per unit time $/m^2 s$.

The photon flux density is related to the optical power (P_{opt}) as

$$\phi = \frac{P_{opt}(1 - R)}{Ah\vartheta} \tag{3.11}$$

where R is the Fresnel reflection coefficient, ϑ is the frequency of incident radiation.

$\alpha(\lambda)$ is the absorption coefficient $(/m)$ which is a function of wavelength.

Here R_n, R_p are the recombination rates of electrons and holes respectively and can be expressed as

$$R_n = \frac{n_p - n_{po}}{\tau_n} \tag{3.12}$$

$$R_p = \frac{p_n - p_{no}}{\tau_p} \tag{3.13}$$

where n_p, p_n are the minority carrier concentrations of electrons and holes in the p-side and n-side respectively, n_{po}, p_{no} represent the carrier concentrations of electron and holes in equilibrium, τ_n and τ_p stands for the minority carrier lifetime of electrons and holes respectively.

Under steady state conditions, the carrier concentrations do not change with time.

Under a d.c steady condition

$$\frac{\partial p}{\partial t} = 0 \tag{3.14}$$

$$\frac{\partial n}{\partial t} = 0 \tag{3.15}$$

In the ATLAS simulation, the simulator uses both the continuity equations by default in computation of current in the semiconductor devices.

3.3.3 Transport Equations

In any semiconductor, the simplest transport model for obtaining the current densities is the drift-diffusion model as it is limited to only three independent variables n, p and ψ.

The expressions for the current the densities using drift-diffusion model under constant electric field region condition are expressed as

$$J_n = qn\mu_n\mathcal{E}_n + qD_n\nabla n \tag{3.16}$$

$$J_p = qp\mu_p\mathcal{E}_p - qD_p\nabla p \tag{3.17}$$

where J_n and J_p are the current densities of electrons and holes, μ_n and μ_p are the electron and hole mobilities, D_n and D_p represents the electron and the hole diffusion constants, $\mathcal{E}_n$ and $\mathcal{E}_p$ are the local electric fields for electrons and holes, ∇n and ∇p represents the three-dimensional spatial gradient of electrons and holes respectively.

The equations (3.16) and (3.17) are valid for the low electric fields. At sufficiently high electric fields, the terms $\mu_n\mathcal{E}_p$ and $\mu_p\mathcal{E}_p$ are replaced by the saturation velocity v_{ns} and v_{ps}. Therefore, the current density can be expressed as

$$J_n = qnv_{ns} + qD_n\nabla n \tag{3.18}$$

$$J_p = qpv_{ps} + qD_p \nabla \mathrm{p} \tag{3.19}$$

The local electric fields are given by

$$\mathcal{E}_n = -\nabla\left(\psi + \frac{kT}{q} ln\, n_i\right) \tag{3.20}$$

$$\mathcal{E}_p = -\nabla\left(\psi - \frac{kT}{q} ln\, n_i\right) \tag{3.21}$$

where E_g is the energy bandgap, T represents the temperature in Kelvin, k represents the Boltzmann's constant.

The expression for the intrinsic carrier concentration (n_i) is given by

$$n_i = \sqrt{N_C N_V} exp\left(\frac{-E_g}{2kT}\right) \tag{3.22}$$

where N_C and N_V are the effective density of states in conduction band and valence band. They are given by

$$N_C = 2\left(\frac{2\pi m_n^* kT}{h^2}\right)^{\frac{3}{2}} \tag{3.23}$$

$$N_V = 2\left(\frac{2\pi m_p^* kT}{h^2}\right)^{\frac{3}{2}} \tag{3.24}$$

The drift diffusion model given in the ATLAS simulation is derived, on the assumption that the Einstein's relation holds good. The diffusion coefficients are estimated as follows

$$D_{n,p} = \frac{kT}{q} \mu_{n,p} \tag{3.25}$$

For any device, the ATLAS simulation involves solving of the above equations numerically following the appropriate boundary conditions.

Optical characterization involves source of light beam to be incident on the device. The current under illumination and the optical characteristics can be computed from the expressions given in the equations (3.26) & (3.27).

For optical characterization, LUMINOUS, an integral part of the ATLAS tool is used to determine the photogeneration in the structure at each mesh point. It uses ray tracing method which performs two calculations simultaneously to obtain the optical intensity using refractive index (n) and the extinction coefficient (k) to find the absorption at each mech point in the device. The two calculations provide the wavelength dependent photogeneration in the photodetector.

The Luminous tool does not compute the optical characteristics like quantum efficiency, responsivity directly. Instead, it uses the currents which are generated during the simulation to calculate the optical characteristics.

The simulation uses monochromatic source of light and the expression for the source photocurrent is given by

$$I_s = q\frac{B_n\lambda}{hc}W_t \tag{3.26}$$

where B_n is the intensity of the beam number n, λ represents the source wavelength, W_t is the width of the beam, c is the velocity of light.

The available photocurrent in the device is expressed as follows

$$I_A = q\frac{B_n\lambda}{hc}\sum_{i=1}^{N_R} W_R \int_0^{Y_i} P_i\alpha_i e^{-\alpha_i y}dy \tag{3.27}$$

where W_R is the width of the ray, α_i is the absorption coefficient in the material, N_R is the number of rays traced, P_i is the attenuation before the ray starts, Y_i is the length of the ray.

3.4 Material Parameters

The photodetector characteristics are determined using the empirical formulae for material parameters as given in the Table 3.1. The mole fraction value of the composition of cadmium (x) is taken to be 0.175325 to obtain a bandgap corresponding to 30 µm wavelength. Most of the material parameters are taken from reference [107].

Table 3.1 Material Parameters

Parameter	**Value**
Energy bandgap (E_g) (eV) [107]	$-0.302 + 1.93x - 0.810x^2 + 0.832x^3 + 5.35 \times 10^{-4}(1-2x)\left\{\frac{-1822 + T^3}{255.2 + T^2}\right\}$
Intrinsic Carrier Concentration (n_i) (m^{-3}) [125]	$(5.24256 - 3.57290x - 4.74019 \times 10^{-4}T + 1.25942 \times 10^{-2}xT - 5.77046x^2 - 4.24123 \times 10^{-6}T^2) \times 10^{20} E_g^{\frac{3}{4}} T^{\frac{3}{2}} exp\left(-\frac{E_g}{2kT}\right)$
Electron Mobility (μ_n) (m^2/Vs) [126]	$\frac{9 \times 10^4 s}{T^{2r}}$
Hole Mobility (μ_p) (m^2/Vs) [126]	$\mu_o\left[1 + \left(\frac{p}{1.8 \times 10^{23}}\right)^2\right]^{-\frac{1}{4}}$
Static Dielectric constant (ϵ_s) [107]	$20.5 - 15.6x + 5.7x^2$

High frequency Dielectric constant (ε_∞) [107]	$15.2 - 15.6x + 8.2x^2$
Electron affinity (χ) (eV) [107]	$4.23 - 0.813 \times (\mathrm{E_g} - 0.083)$
Effective Mass of electrons (m_n^*) (Kg) [111]	$m_0\left(1 + 2F + \frac{E_p}{3}\left(\frac{2}{E_g} + \frac{1}{E_g + \Delta}\right)\right)^{-1}$
Effective Mass of holes (m_p^*) (Kg) [111]	$0.55m_0$
Absorption Coefficient (α) (m^{-1}) [113], [127]	$\alpha_0 exp\left(\frac{\delta(E - E_0)}{kT}\right)$

3.5 Modeling of Carrier lifetime

In order to determine the dark current, appropriate calculation of drift and diffusion components is necessary. Modeling of the minority carrier lifetimes must be performed taking into consideration all the possible recombination mechanisms such as Shockley-Read-Hall (SRH) process, radiative process, and non-radiative Auger recombination. Improvement in the fabrication procedures reduces SRH recombination. In the detectors made of narrow bandgap materials, Auger and radiative mechanisms are dominant.

3.5.1 Radiative Mechanism

It is an intrinsic mechanism and depends on the electron band structure of the material. The radiative process takes place when free electrons and holes recombine, emitting the excess energy in the form of a photon. The recombination rate (G_R) can be expressed through the equation [107]

$$G_R = \frac{8\pi}{h^3 c^3} \int_0^\infty \frac{\epsilon(h\vartheta)\alpha(h\vartheta)E^2 dE}{exp\left(\frac{E}{kT}\right) - 1} \tag{3.28}$$

where $\alpha(h\vartheta)$ represents the absorption coefficient, $\epsilon(h\vartheta)$ is the relative dielectric constant and c, h, k, T represent the velocity of light, Planck's constant, Boltzmann's constant, the temperature in Kelvin respectively.

The lifetime due to radiative process using the high-frequency dielectric constant value ϵ_∞ and neglecting the dispersion in dielectric constant can be written as [107]

$$\tau_{RAD} = \frac{n_i^2}{G_R(n_0 + p_0)} \tag{3.29}$$

where n_i is the intrinsic carrier concentration, n_0, p_0 represent the thermal equilibrium concentrations of electrons and holes respectively.

The expression for the dependence of α on E as analyzed and given as [107]

$$\alpha(E) = \frac{2^{2/3} m_0 q^2}{3\varepsilon_\infty^{1/2}(\hbar)^2}\left(\frac{m_n^* m_p^*}{m_0\left(m_n^* + m_p^*\right)}\right)^{3/2}\left(1 + \frac{m_0}{m_n^*} + \frac{m_0}{m_p^*}\right)\left(\frac{E - E_g}{m_0 c^2}\right)^{1/2} \tag{3.30}$$

where $\hbar = h/2\pi,\ E = h\vartheta.$

On the assumption of $E_g(eV) > \frac{kT}{q}$ and ignoring the dispersion in the dielectric, we can rewrite G_R as given in [107]

$$G_R = 5.8 \times 10^{-13} n_i^2 \epsilon_\infty^{\frac{1}{2}} \left(1 + \frac{m_0}{m_n^*}\right)\left(\frac{m_0}{(m_n^* + m_p^*)}\right)^{\frac{3}{2}}\left(\frac{300}{kT}\right)^{\frac{3}{2}}\left(E_g^2 + 3kTE_g + 3.75k^2T^2\right) \tag{3.31}$$

3.5.2 Shockley Read Hall Mechanism

The Shockley-Read Hall (SRH) mechanism is not an intrinsic process, as it occurs via levels in the forbidden energy gap. It is not a fundamental limit to photodetector performance. It may be reduced by lowering the concentrations of native defects and foreign impurities. In the SRH mechanism, the generation and the recombination occur via energy levels introduced by impurities or lattice defects into the forbidden energy gap. As recombination centers, they trap electrons and holes. As the generation centers, they successively emit them. The rates of the generation and the recombination depend on the individual nature of the center and its predominant occupation state of the charge carriers as well as on the local densities of those carriers in the bands of the semiconductor.

The carrier lifetime due to SRH recombination is given as [107]

$$\tau_{SRH} = \frac{1}{\sigma N_t v_{th}} \tag{3.32}$$

where σN_t represents the capture cross-section trap density product, v_{th} represents the thermal velocity of the minority carriers in the active region and is expressed as

$$v_{th} = \sqrt{\frac{3kT}{m^*_{n,p}}} \tag{3.33}$$

3.5.3 Auger Mechanism

The Auger recombination is considered to be a band-to-band recombination process but it is not accompanied by the emission of photons. Therefore, it is considered as a non-radiative process. In this process, an electron recombines with a hole by giving up excess energy to another carrier instead of releasing a photon. This means that in the Auger recombination process, the excess energy from the electron-hole recombination is transferred to another electron or hole which is subsequently excited to higher energy states within the same band instead of giving off photons. The additional particle absorbs the momentum and energy of the colliding particle and helps to satisfy the conservation of momentum necessary for the successful recombination. It is also be viewed as the reverse process of impact ionization. Auger recombination in semiconductors is called as a three-particle process where three carriers, e.g., two electrons and a hole or two holes and one electron participate in the process. The Auger recombination is a dominant process in the narrow bandgap semiconductor materials. It becomes more dominant as the temperature increases and becomes crucial at or near room temperature. It is understood that the Auger mechanism is most likely to impose the fundamental limit to the performance of photovoltaic detectors, based on narrow bandgap materials. There are several types of Auger recombination in a semiconductor. Out of which three processes are dominant in the narrow bandgap materials. Auger-1 is prevalent in n-type, Auger-7 is dominant in p-type materials whereas Auger-S process may be neglected for narrow bandgap materials with energy bandgap less than spin split-off energy ($\Delta = 1\ eV$). Therefore, for the $Hg_{1-x}Cd_xTe$ material only Auger-1 and Auger-7 are to be considered [128].

The net Auger lifetime is given as

$$\frac{1}{\tau_{AU}} = \frac{1}{\tau_{A1}} + \frac{1}{\tau_{A7}} \tag{3.34}$$

where τ_{A1} and τ_{A7} are the carrier lifetimes involving Auger-1 and Auger-7 processes respectively.

Auger-1 carrier lifetime is given by

$$\tau_{A1} = \frac{2n_i^2}{n_0(n_0 + p_0)}\tau_{A1}^{(i)} \tag{3.35}$$

Auger-7 carrier lifetime is given by

$$\tau_{A7} = \frac{2n_i^2}{p_0(n_0 + p_0)} \gamma \tau_{A1}^{(i)} \tag{3.36}$$

where

$$\gamma = \frac{\tau_{A7}^{(i)}}{\tau_{A1}^{(i)}}$$

$\tau_{A1}^{(i)}$ is the Auger lifetime for intrinsic material and is given by

$$\tau_{A1}^{(i)} = 3.8 \times 10^{-18} \varepsilon_s^2 \frac{m_0}{m_n^*} \left(1 + \frac{m_n^*}{m_p^*}\right)^{1/2} \left(1 + 2\frac{m_n^*}{m_p^*}\right) \left(\frac{E_g}{kT}\right)^{3/2} exp\left(\frac{1 + 2\frac{m_n^*}{m_p^*}}{1 + \frac{m_n^*}{m_p^*}} \frac{E_g}{kT}\right) |F_1 F_2|^{-2} \tag{3.37}$$

where

$|F1F2|$ is the overlap integral.

Taking into consideration all the recombination mechanisms that affect the carriers, the effective lifetime (τ_{eff}) can now be written as:

$$\frac{1}{\tau_{eff}} = \frac{1}{\tau_{RAD}} + \frac{1}{\tau_{AU}} + \frac{1}{\tau_{SRH}} \tag{3.38}$$

3.6 Dark Current Modeling

The dark current of the photodetector has been modeled taking into effect all the mechanisms occurring in the various regions of the detector, neglecting the current due to drift mechanism. In the dark current modeling surface recombination need to be taken as it is prevalent at the surface/heterointerface and its importance is explained in detail below.

The recombination mechanisms radiative, SRH and Auger discussed earlier are bulk recombination processes. These processes occur within volume of the material. Another recombination namely surface recombination is more prevalent in the heterojunction photodetectors. In this chapter, the proposed photodetector consists of a hetero-interface between CdTe and HgCdTe. Any lattice mismatch between the two materials at the hetero-interface creates traps and as a result, the effect of the surface recombination may take place. Due to the lattice mismatch between the materials, in this case CdTe is only 0.3% larger than $Hg_{1-x}Cd_xTe$, the effect of surface recombination is present in the structure but somewhat less in nature. Hence, it is necessary to consider its effect on the boundary conditions. It is normally characterized in terms of the parameter called surface recombination velocity (S). A perfect interface is one for which the surface recombination is zero ($S = 0$). If S is very high value, it indicates that the quality of the surface is very bad which is undesirable.

We have solved the continuity equation to compute the dark current using the following boundary conditions as shown in Fig.3.1

$$I_p(x)\big|_{x=0} = -qAS_p\delta p_n(0) \tag{3.39}$$

$$\delta p_n(x)|_{x=t-x_n} = p_{no}\left(\exp\left(\frac{qV}{kT}\right) - 1\right) \tag{3.40}$$

$$\delta n_p(x)\big|_{x=t+x_p} = n_{po}\left(\exp\left(\frac{qV}{kT}\right) - 1\right) \tag{3.41}$$

$$I_n(x)|_{x=t+d_p} = qAS_n\delta n_p\left(t + d_p\right) \tag{3.42}$$

where S_p is the recombination velocity of holes at $n^+ - CdTe$ and $n^0 - Hg_{1-x}Cd_xTe$ interface and S_n is the recombination velocity of electrons respectively, δp_n and δn_p corresponds to excess carrier concentrations, n_{po} and p_{no} being the equilibrium carrier concentration values.

3.6.1 Diffusion currents

In the structure under consideration, diffusion current is dominated by the injection of holes from p^+ region in the active region and is given by

$$\left(I_p\right)_n = \frac{qn_i^2 A}{N_D}\frac{D_p}{L_p}\left\{\frac{\frac{S_pL_p}{D_p}cosh\left(\frac{t-x_n}{L_p}\right) - sinh\left(\frac{t-x_n}{L_p}\right)}{cosh\left(\frac{t-x_n}{L_p}\right) - \frac{S_pL_p}{D_p}sinh\left(\frac{t-x_n}{L_p}\right)}\right\}\left(exp\left(\frac{qV}{kT}\right) - 1\right) \tag{3.43}$$

where A is the area of the device, N_D represents the donor concentration in the active region, L_p is the diffusion length, τ_p is the lifetime of holes in n^0 region, t is the thickness of active region, x_n is the width of the depletion region in n^0 region.

Similarly, for accurate analysis, the injection of electrons from the n^0 region in the p^+ region is also being considered and is given by

$$(I_n)_p = \frac{qn_i^2 A}{N_A}\frac{D_n}{L_n}\left\{\frac{\frac{S_nL_n}{D_n}cosh\left(\frac{d_p-x_p}{L_n}\right) - sinh\left(\frac{d_p-x_p}{L_n}\right)}{cosh\left(\frac{d_p-x_p}{L_n}\right) - \frac{S_nL_n}{D_n}sinh\left(\frac{d_p-x_p}{L_n}\right)}\right\}\left(exp\left(\frac{qV}{kT}\right) - 1\right) \tag{3.44}$$

where N_A is the acceptor concentration, L_n is the diffusion length, x_p is the width of the depletion region in p^+ region, τ_n is the electron lifetime in p^+ region, d_p is the thickness of p^+-region.

Therefore, the total diffusion current is given by

$$I_{DIFF} = \left(I_p\right)_n + (I_n)_p \tag{3.45}$$

3.6.2 Generation–recombination (G-R) currents

It becomes a major component of the dark current especially in devices like diodes that contain defects in the depletion regions. These defects may be inherent in the material itself. It can be approximated as [129]

$$I_{GR} = \frac{qn_iWVA}{(V_{bi} - V)\tau_{eff}} \quad for\ V < 0 \tag{3.46}$$

$$I_{GR} = \frac{2n_iWkTA}{(V_{bi} - V)\tau_{eff}} sinh\left(\frac{qV}{kT}\right) \quad for\ V > 0 \tag{3.47}$$

where $W = x_n + x_p$ is the width of the depletion region, V_{bi} is the built-in potential.

3.6.3 Tunneling currents

Trap assisted tunneling (TAT) usually occurs in devices operating at low reverse bias conditions. It occurs at the edges of the depletion region due to crossing of minority carriers to the empty states in the other side of the junction [129]. In the narrow bandgap materials, band-to-band (BTB) tunneling current arises due to the tunneling of the carriers at high reverse bias. This is not much significant as the p-i-n photodetectors are usually operated at relatively lower reverse bias [129].

$$I_{TAT} = \frac{q^3 m_n^* \mathcal{E}_m M^2 W N_t A}{8\pi\hbar^3 (E_g - E_t)} exp\left(-\frac{4\sqrt{2m_n^*(E_g - E_t)^3}}{3q\hbar E}\right) \tag{3.48}$$

$$I_{BTB} = \frac{q^3 \mathcal{E}_m V A}{4\pi^2 \hbar^2} \sqrt{\frac{2m_n^*}{E_g}} exp\left(-\frac{4\sqrt{2m_n^* E_g^3}}{3q\hbar} \right) \tag{3.49}$$

where $\mathcal{E}_m$ is the maximum electric field in the depletion region, N_t is the trap density, M corresponds to matrix element related to trap potential, E_t is the energy of trap center, $\hbar = \frac{h}{2\pi}$.

3.6.4 Quantum Efficiency Modeling

In the computation of quantum efficiency, primarily we consider the components arising from the depletion region and the quasi-neutral regions of the photodetector.

The electron-hole pairs are generated at a rate given by

$$G_p(x) = \frac{\alpha_p(\lambda)(1 - R_{n^+})(1 - R_{n^0})\left(1 - R_{p^+}\right)P_{opt}}{Ah\nu} exp\left(-\alpha_p(\lambda)x\right) \tag{3.50}$$

$$G_n(x) = \frac{\alpha_n(\lambda)(1 - R_{n^+})(1 - R_{n^0})P_{opt}}{Ah\vartheta} exp(-\alpha_n(\lambda)x) \tag{3.51}$$

where $\alpha_p(\lambda)$, $\alpha_n(\lambda)$ are the absorption coefficients, P_{opt} represents the optical power of the incident radiation.

The Fresnel's reflection coefficients have been calculated at different surfaces using the formula as given below

$$R_{n^o,n^+p^+} = \frac{(n_t - n_e)^2}{(n_t + n_e)^2} \tag{3.52}$$

where n_t represents the refractive index of the transmitting medium and n_e represents the refractive index of the entrance medium.

Solving the continuity equation following the boundary conditions described in the dark current modeling section, the expressions for the quantum efficiencies are obtained as derived in [129]. The total quantum efficiency (η) including the contributions from the neutral regions and the depletion region is given by

$$\eta = \eta_n + \eta_P + \eta_{dep} \tag{3.53}$$

where η_n, η_P, η_{dep} are the quantum efficiencies in the neutral n-region, neutral p-region and the depletion regions respectively.

3.6.5 Modeling of Specific detectivity

The most important figure of merit of the photodetector for use in the communication system is the specific detectivity D^*, which depends on the wavelength of incident light (λ), the quantum efficiency (η) and net resistance area product $(RA)_{NET}$. As the dark current of the detector is contributed by three major components e.g., diffusion, generation-recombination and tunneling (which includes trap assisted tunneling (TAT) and band to band tunneling (BTB)), the detectivity of the photodetector under consideration should be estimated from the net value of RA product arising out of these mechanisms and is given as

$$Specific\ Detectivity(D^*) = \frac{q\eta\lambda}{hc}\sqrt{\frac{(RA)_{NET}}{4kT}} \tag{3.54}$$

3.6.6 Modeling of Current Responsivity

The responsivity ($\Re$) of the photodiode is the ratio of the photocurrent (I_{ph}) to the incident optical power (P_{opt}). It is expressed in terms of *A/W* and is given by

$$\Re = \frac{I_{ph}}{P_{opt}} \tag{3.55}$$

$$Responsivity(\Re) = \frac{q\eta\lambda}{hc} \tag{3.56}$$

3.6.7 Noise Equivalent Power

It is the most critical metric that determines the sensitivity of the photodetector. It is the minimum power required at the input source to produce a signal to noise ratio of one at the output in a unity bandwidth system. The NEP is affected by the different types of thermal noises as well the noise generated due to optical excitation.

$$NEP = \frac{\sqrt{A\ B}}{D^{*}} \tag{3.57}$$

3.7 Results and Discussion

ATLAS™ TCAD tool has been utilized for the numerical simulation. The doping in all the regions is assumed to be uniform. In the simulation, ANALYTIC model is used for mobility computation. All the recombination mechanisms AUGER, SRH, OPTICAL have been considered for dark current. For tunneling mechanism, standard band-to-band is considered. In both analytical model and ATLAS simulation, surface recombination occurring at the heterojunction interface and contacts are also considered. The device is simulated and studied with respect to electrical and optical characteristics. For the dark current, carrier modeling has been done separately in MATLAB. The carrier lifetimes thus obtained have been utilized for the numerical simulation in ATLAS™. A separate program has been developed in MATLAB for computation of absorption coefficient using Kane model. A file containing the refractive index (n) and the extinction coefficient (k) data was made using the above obtained absorption coefficients for various wavelengths. For the optical characterization, the file containing the (n, k) data is incorporated in the DECKBUILD code for ATLAS simulation.

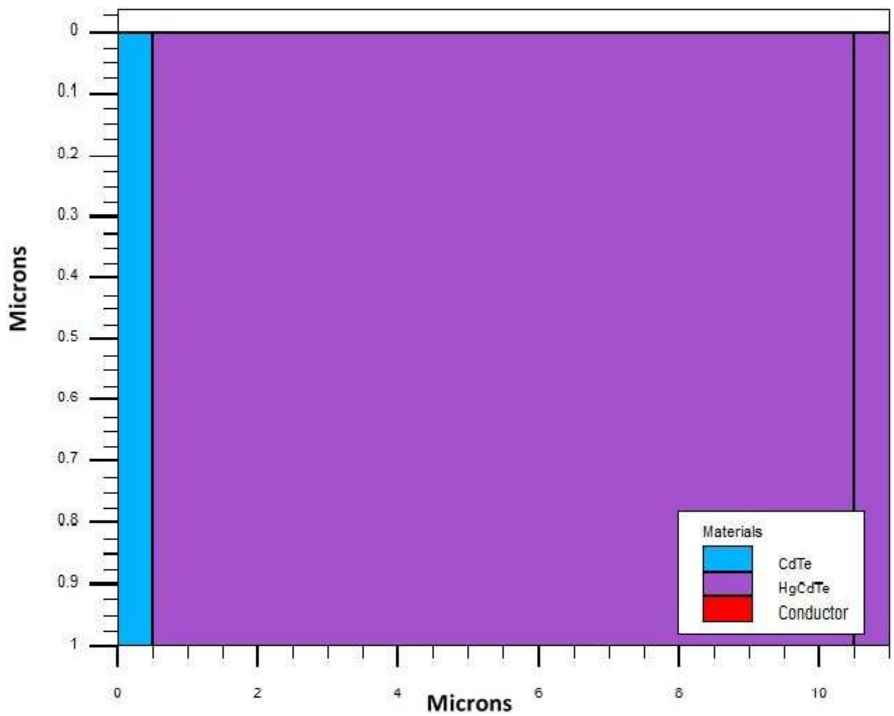

Fig.3.2 N^{+}-i-p^{+} photodetector structure simulated in ATLAS

The doping of the window layer is taken as $1 \times 10^{24}\ m^{-3}$, in the active layer $1 \times 10^{21}\ m^{-3}$ and in the p^{+} layer as $1 \times 10^{24}\ m^{-3}$. Also, the values of N_C, N_V are calculated and found to be $5.9242 \times 10^{20}\ m^{-3}$, $1.33 \times 10^{24}\ m^{-3}$ respectively. The incident radiation power is of the order of $10^{4}\ Wm^{-2}$. The effective lifetime of the carriers is found to be $1.35 \times 10^{-7}\ s$. The absorption coefficient for the desired wavelength (30 μm) is calculated to be $1.46478 \times 10^{5}\ m^{-1}$. The penetration depth is the inverse of the absorption coefficient. As its value (6.8 μm) is not so large, any absorption beyond the active region is not required. A set of values containing parameters are included in the DECKBUILD code interfaced with the ATLAS™. The electric characteristics are obtained by BLAZE and the optical characteristics through LUMINOUS interfaced with the ATLAS™. The ATLAS simulated structure of the proposed device is shown in Fig.3.2. The CdTe (window) layer is n-type doped and is 0.5 μm thick so as to act as a transparent window to the incoming radiation. HgCdTe is chosen for active region as well as p^+ region. The composition of the HgCdTe is selected to absorb the desired wavelength (30 μm wavelength in this case). The origin of the distance coordinate is assumed to coincide with the $N^+ - n^0$ junction. The active region and p^+ region thicknesses are chosen to be 10 μm, 0.5 μm respectively. The presence of wider active region accounts for greater photon absorption and thereby improved optical characteristics.

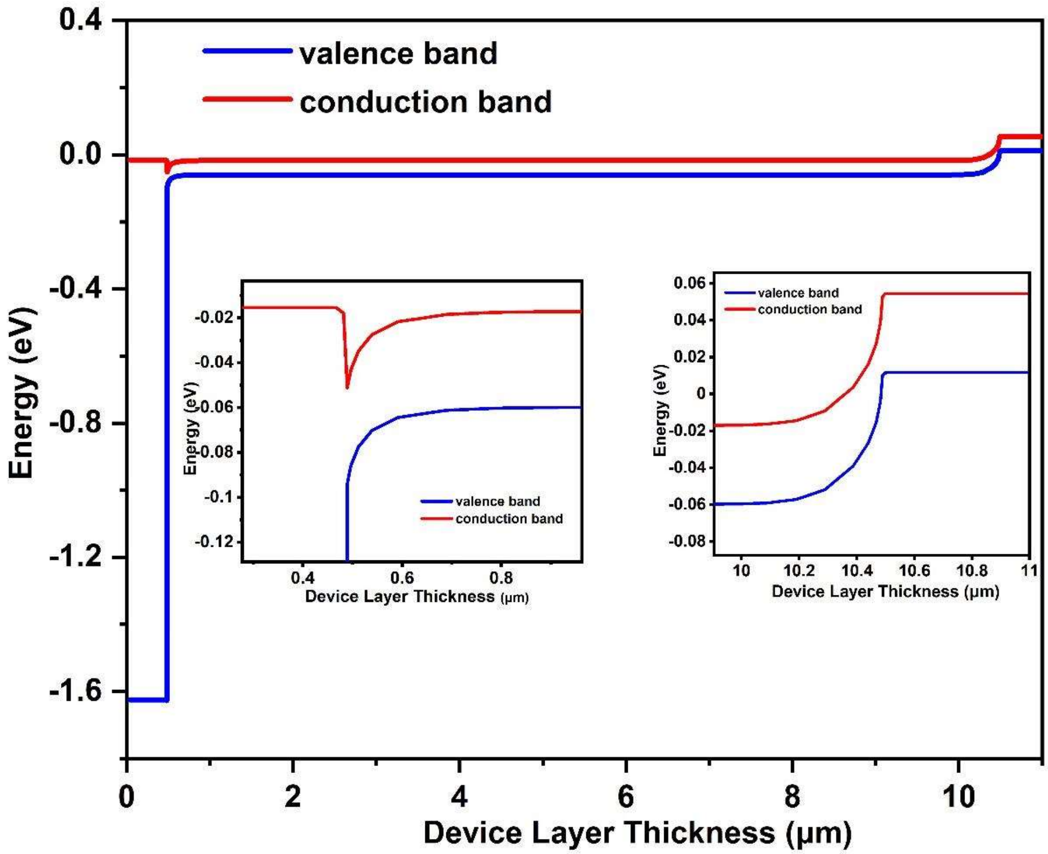

Fig.3.3 Energy band diagram in equilibrium condition

Fig.3.3 shows the energy band diagram of the proposed n-i-p photodetector in equilibrium condition. We can see in the inset of the Fig.3.3 showing the heterojunction and homojunctions formed. A spike is observed at the interface of $N^{+} - CdTe/\ n^{0} - HgCdTe$ due to the formation of heterojunction.

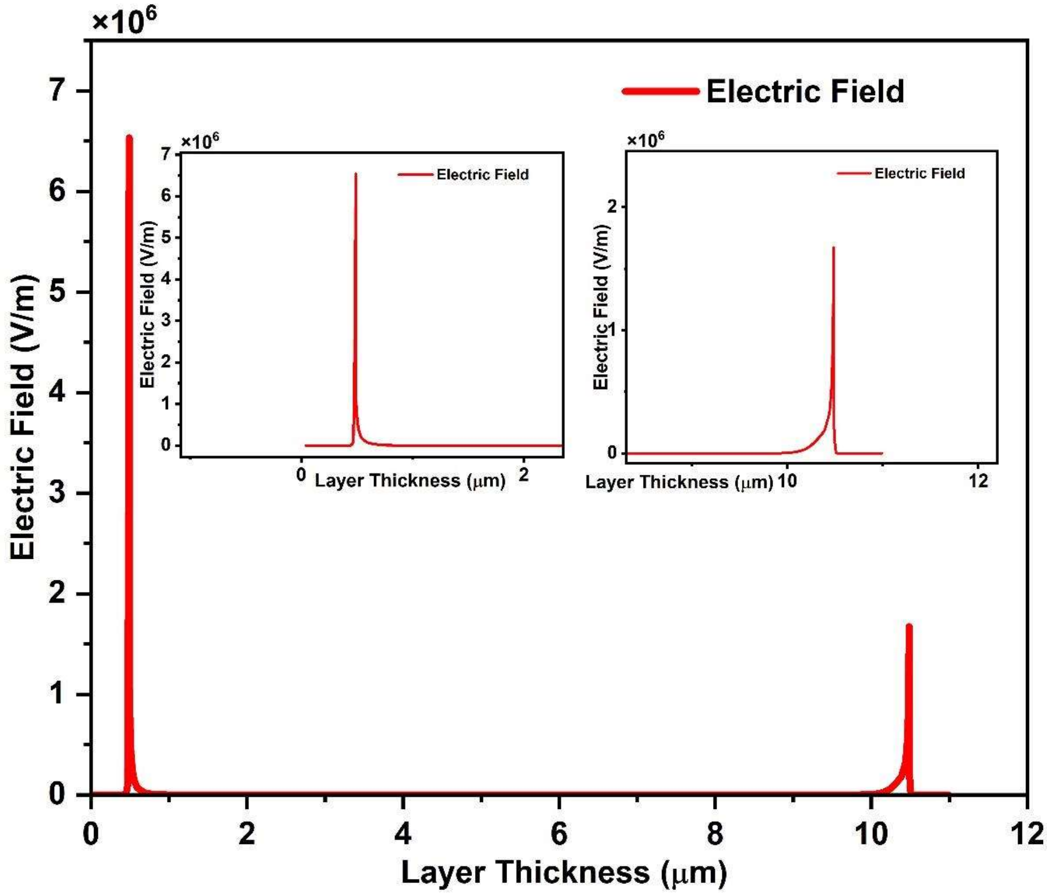

Fig.3.4 Electric field profile of the photodetector under zero bias

In Fig.3.4, a strong electric field is developed at the heterointerface because of the junction formed between $N^{+} - CdTe$ and $n^{o} - HgCdTe$. The electric field at the interfaces have been shown in inset. It is found to have an electric field of $6.53\ X\ 10^{6} V/m$ at the hetero-junction and $1.6\ X\ 10^{6} V/m$ at the homojunction.

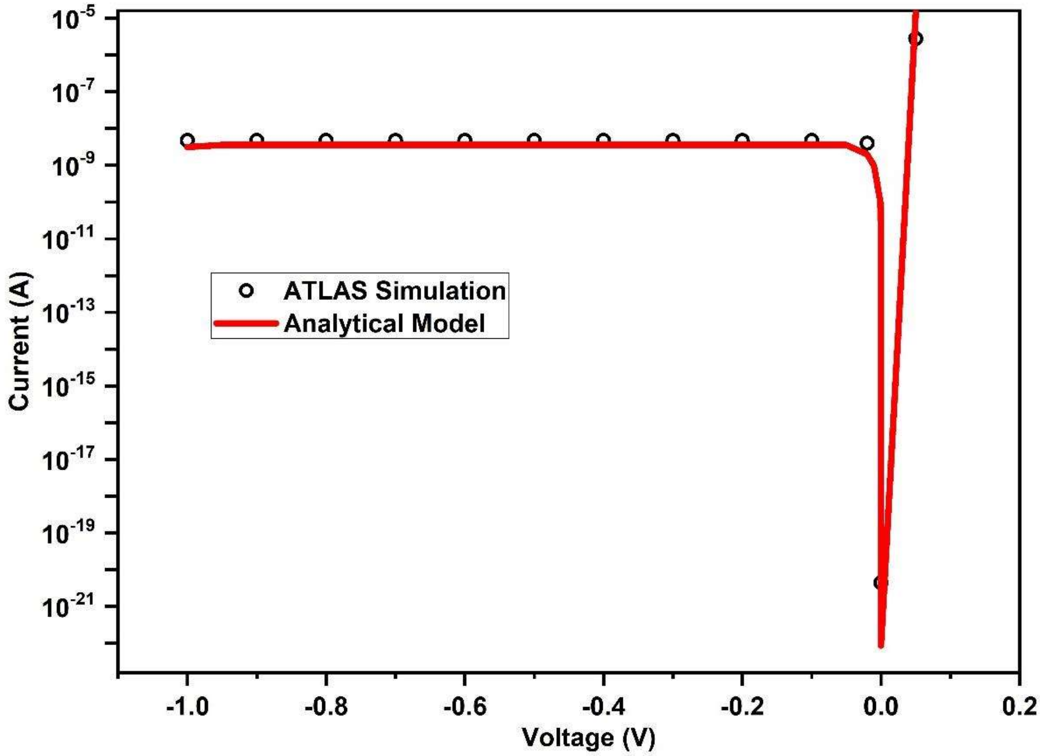

Fig.3.5 Dark current versus applied voltage

Fig.3.5 shows the changes in the dark current with respect to the applied voltage. It is evident that the dark current obtained from the ATLAS simulation is almost matching with the dark current from the analytical model. The photodetector designed shows a dark current of $4.6 \times 10^{-9}\ A$ at a reverse bias of 0.5 V.

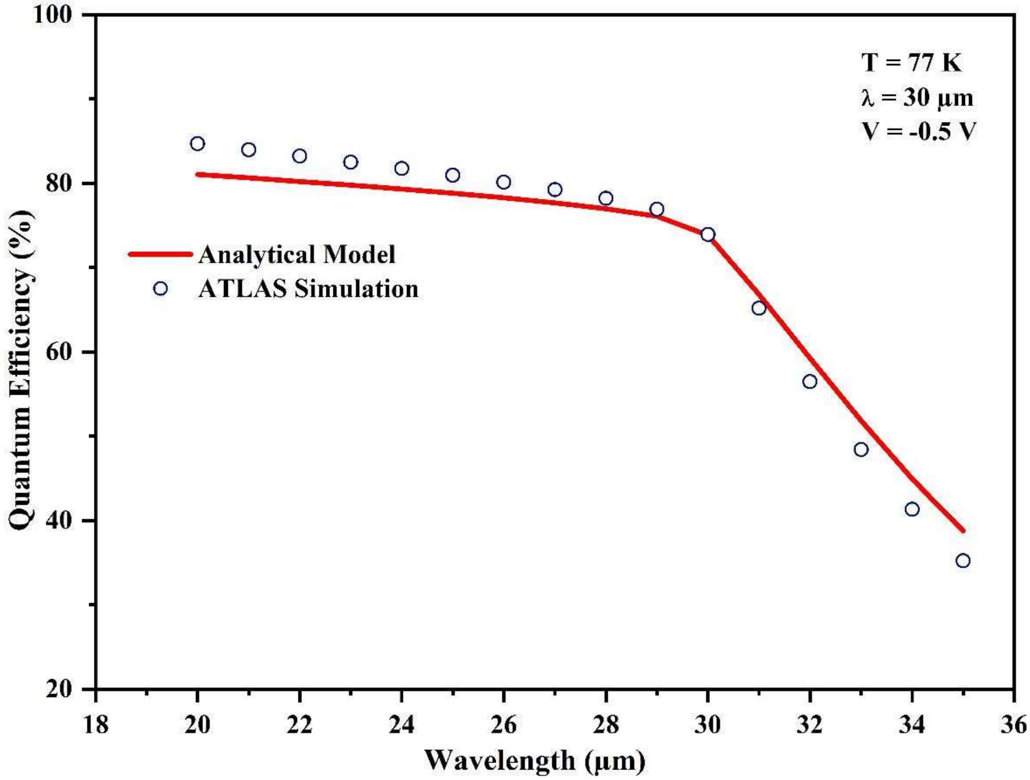

Fig.3.6 Variation of quantum efficiency versus wavelength at a reverse bias of V=0.5 V

The wider active layer of the proposed photodetector accounts for absorption of a greater number of photons thereby increased quantum efficiency of ~73.93% as shown in Fig.3.6. The quantum efficiency falls rapidly beyond cut-off wavelength owing to high photon absorption in the neutral regions. From the Fig.3.6, it is evident that the results obtained from the ATLAS simulation are almost matching with the results obtained using the analytical model.

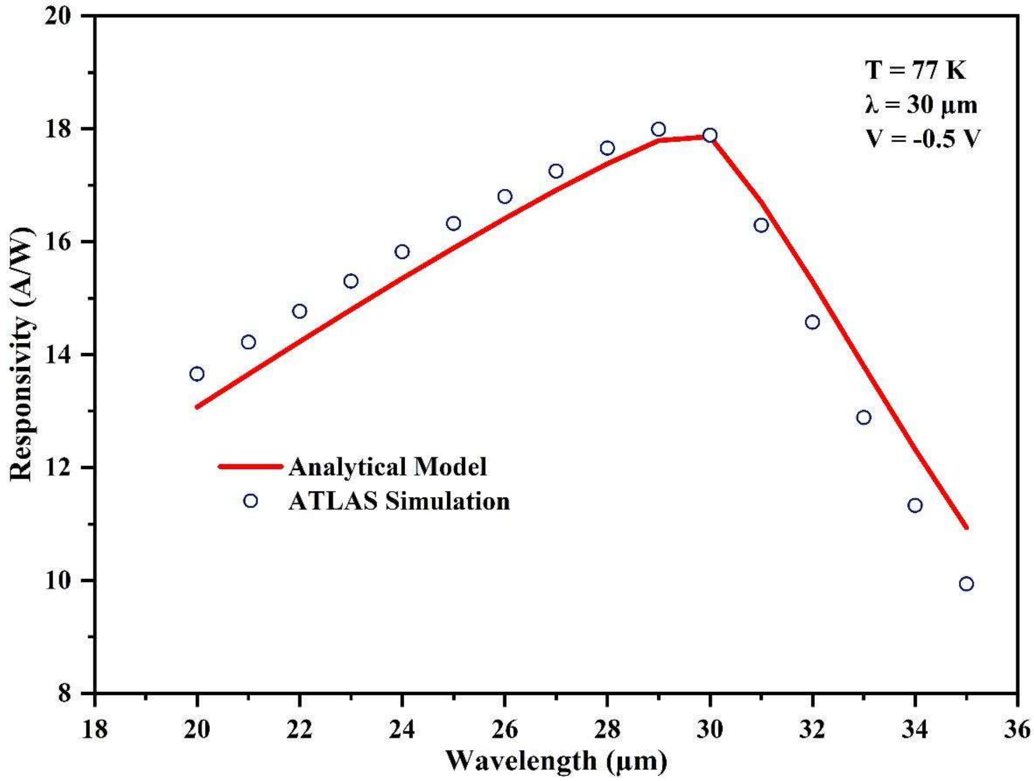

Fig.3.7 Variation of responsivity versus wavelength at a reverse bias of V=0.5 V

Fig.3.7 shows the variation of responsivity of the photodetector with the wavelength. The quantum efficiency (η) is a function of absorption coefficient (α), and responsivity is directly proportional to η. As α decreases beyond the cut-off wavelength, so does the quantum efficiency. Therefore, responsivity falls beyond the cut-off wavelength which is evident from the Fig.3.7. The photodetector exhibits a responsivity of ~17.9 A/W. It is apparent from the figure that the results obtained from the ATLAS simulation are in close agreement with the results from the analytical model.

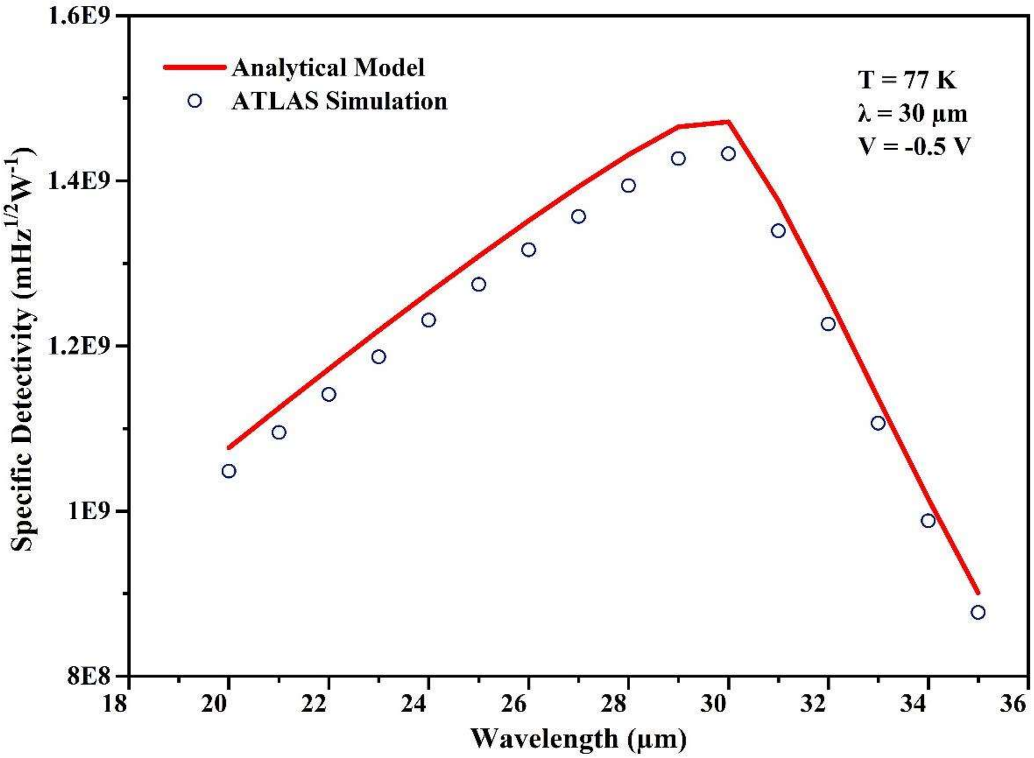

Fig.3.8 Variation of specific detectivity versus wavelength at a reverse bias of V=0.5 V

It is seen from the Fig.3.8 that the photodetector shows a peak specific detectivity of $1.44 \times 10^9\ mHz^{1/2}$ at the cut-off wavelength of 30 µm. The detectivity falls very slowly at shorter wavelengths and declines rapidly beyond the cut-off wavelength. The detectivity is not high in comparison to that of the LWIR photodetectors. Due to the narrow bandgap of the material, the detectivity of the device is significantly affected by the noise. From the Fig.3.8, we can see that the results of ATLAS simulation are in good agreement with the analytical model.

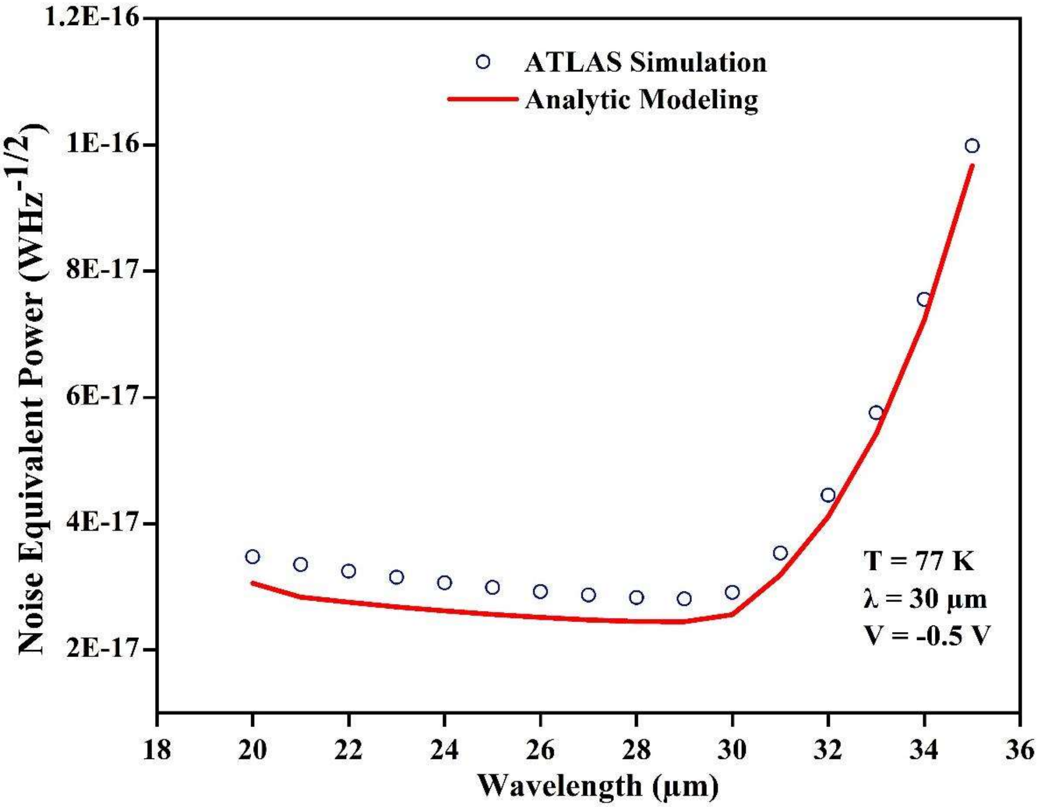

Fig.3.9 Variation of Noise equivalent power (NEP) versus wavelength at a reverse bias of V=0.5 V

Fig.3.9 shows the variation of NEP of the photodetector with the wavelength. It can be seen from the figure that the photodetector has a very small value of NEP ~$0.3 \times 10^{-16}\ WHz^{-\frac{1}{2}}$ at a wavelength of 30 µm. We can see an increase in the value of NEP at longer wavelengths and a very less drop below cut-off wavelength.

3.8 Conclusion

In this chapter, a $N^{+} - CdTe/\, n^{0} - Hg_{0.824675}Cd_{0.175325}Te\ /p^{+} - Hg_{0.824675}Cd_{0.175325}Te$ n-i-p photodetector has been proposed for terahertz application. Since the experimental costs involved in development of photodetectors at the terahertz frequencies are very high, the theoretical and simulation studies presented in this chapter may be considered by design engineers. The results obtained from ATLAS™ simulation are compared and contrasted for the validation with those obtained on the basis of the analytical model. The results obtained on the basis of ATLAS simulation are in good agreement with the analytical results indicating the validity of the model considered. The device has been operated at a wavelength of 30 µm, a bias voltage of 0.5 V and at a temperature of 77 K. It is found to exhibit a low dark current, high values of quantum efficiency, responsivity, and specific detectivity with an ultra-low noise-equivalent power (NEP) and is expected to find applications as a sensitive THz detector.